Journal of Materials Chemistry C

ROYAL SOCIETY OF CHEMISTRY

PAPER

View Article Online
View Journal | View Issue

Cite this: J. Mater. Chem. C, 2021, 9, 7753

Pentagonal two-dimensional noble-metal dichalcogenide PdSSe for photocatalytic water splitting with pronounced optical absorption and ultrahigh anisotropic carrier mobility†

Feng Xiao,[a] Wen Lei,[ab] Wei Wang,[a] Lili Xu,[c] Shengli Zhang *[c] and Xing Ming *[ad]

Emerging two-dimensional (2D) noble-metal dichalcogenide (NMDC) PdX_2 (X = S and Se) materials crystallize in an unusual orthorhombic structure (2O phase) with unique pentagons and PdX_4 planar squares as building blocks, and have attracted tremendous attention in recent years for their novel physical and chemical properties, as well as promising applications in the future. Motivated by the attractive properties and encouraging applications of PdX_2 materials, we explore the 2O phase NMDC material PdSSe using particle swarm optimization algorithms combined with first-principles calculations. We not only uncover three stable low-energy bulk phases, but also predict two polymorphs of the 2D monolayer exfoliated from the bulk phases, exhibiting mechanical, dynamic, and thermal stabilities. Due to its novel puckered pentagonal structure, the PdSSe monolayer exhibits flexible mechanical properties with anisotropic Young's modulus and Poisson's ratio. The bandgaps of the two polymorphs of the 2D pentagonal PdSSe monolayer are 2.10 and 2.06 eV, and their band-edges perfectly straddle the redox potential of water. Furthermore, these materials possess excellent light absorption in the visible and ultraviolet regions, and the absorption coefficients reach the order of 10^6 cm^{-1}. More importantly, the predicted materials exhibit highly desirable carrier mobilities and anisotropy, which can promote the separation of the photogenerated electrons and holes, and effectively reduce the probability of recombination, thus remarkably promoting photocatalytic water splitting. These excellent properties enable PdSSe monolayers as candidate materials for promising applications in high-performance optoelectronic and nanoelectronic devices. The predicted unconventional properties of PdSSe not only supply a meaningful complement to the fascinating NMDC materials of $PdSe_2$ and PdS_2, but also will attract extensive interest from a wide audience to explore unanticipated properties and design new functional devices based on PdSSe.

Received 18th March 2021,
Accepted 17th May 2021

DOI: 10.1039/d1tc01245b

rsc.li/materials-c

I. Introduction

The discovery of monolayer two-dimensional (2D) graphene opened a new era of materials science.[1] Unfortunately, the absence of a band gap in graphene is a major hindrance to its practical applications.[2] Inspired by the prospective applications of 2D graphene materials, intensive efforts have been devoted to seeking other alternative 2D semiconducting materials. Numerous 2D layered materials have been explored by theoretical predictions and experimental realization.[3] Among them, transition metal dichalcogenide (TMDC) materials, as potential candidates for next generation spintronic, nanoelectronic, thermoelectric, and optoelectronic applications, have attracted much interest.[4–6] Particularly, layered noble-metal dichalcogenide (NMDC) MX_2 (M = Pt, Pd, X = S, Se, Te) materials have drawn increasing attention as new members of the 2D material family in recent years. NMDC materials have stimulated abundant applications in spintronics, optoelectronics, sensors, photocatalysts, photodetectors, thermoelectric devices, and field effect transistors.[7–9]

Unlike the well-known hexagonal crystal structure of most familiar TMDC materials (1T or 2H phase), layered NMDC PdX_2 (X = S or Se) materials crystallize in an unusual orthorhombic structure (named the 2O phase) with unique pentagons as

[a] College of Science, Guilin University of Technology, Guilin 541004, P. R. China. E-mail: mingxing@glut.edu.cn
[b] Key Laboratory of Artificial Micro- and Nano-Structures of Ministry of Education and School of Physics and Technology, Wuhan University, Wuhan 430072, P. R. China
[c] MIIT Key Laboratory of Advanced Display Materials and Devices, School of Materials Science and Engineering, Nanjing University of Science and Technology, Nanjing 210094, P. R. China. E-mail: zhangslvip@njust.edu.cn
[d] MOE Key Laboratory of New Processing Technology for Nonferrous Metal & Materials, Guilin University of Technology, Guilin 541004, China

† Electronic supplementary information (ESI) available. See DOI: 10.1039/d1tc01245b

building blocks. In addition, different from the octahedral (1T phase) or trigonal prismatic (2H phase) MX_6 polyhedron in common TMDC materials, Pd atoms are coordinated with four chalcogen atoms to form a PdX_4 planar square in PdX_2 materials.[10] Due to the weak interlayer van der Waals (vdW) forces in the bulk phase, monolayer PdX_2 materials can be exfoliated from their bulk phase according to theoretical predictions.[7,11–16] Experimentally, highly air-stable monolayers and few-layer flakes of PdX_2 have been successfully prepared by mechanical exfoliation, molecular beam epitaxy growth, chemical vapor deposition, and selenization or sulfurization approaches.[17–24] Attributed to their twisted, folded, pentagonal layered structures, PdX_2 materials display novel properties including layer-dependent band gaps,[12,17,24] ambipolar charge transport with high carrier mobility,[17,23,25,26] and excellent thermoelectric performance.[15,18,27,28] The physical and chemical properties of PdX_2 can be dramatically modulated by external stimuli, such as electrical field,[17,25] thermal annealing,[18] gas pressure,[26] electron or plasma irradiation,[29–31] and mechanical strain or pressure.[27,32–36] For example, semiconductor to semimetal transformation under compression, strain-tuned ferroelastic transformation, pressure-induced structural transition from the 2O phase to pyrite phase and concomitant superconductivity have been observed in the bulk phases of PdX_2.[32–36] In addition, the ambipolar charge transport behavior, the thermoelectric properties, and the device performance of field effect transistors can be effectively manipulated by thermal annealing, gas pressure, and electron or plasma irradiation.[18,26,29]

2O phase PdX_2 with a 2D pentagonal layered structure provides a good platform to study structural engineering through defects and chemical substitution. Previous investigations demonstrate that vacancy defects and doping can effectively tailor the structural, electronic, optoelectronic, and catalytic activities of $PdSe_2$.[30,31,37–39] Recently, the structure, optical, and electrical transport characteristics, and thermoelectric properties of $PdSe_{2-x}S_x$ solid solutions with a wide range of x ($0 \leq x \leq 0.86$) have been reported, which suggest that S substitution can be an effective compositional tuning approach to modulate the electronic structure of $PdSe_2$.[40] In fact, as early as 1965, the 2O structure PdSSe was prepared and its energy gap measured experimentally was 0.65 eV.[41] Regrettably, to the best of our knowledge, there has been no experimental report on the detailed crystal structure of bulk phase PdSSe. Even though recently theoretical studies reported the electronic structure, and thermoelectric, photovoltaic, and photocatalytic properties of the monolayer and few-layer PdSSe,[42–44] the artificial assumption of the Janus structure is not exactly consistent with the experimentally reported 2O structure.[40,41] In view of the attractive properties and prospective applications of 2O phase PdX_2 materials, it is highly desirable to determine the ground state crystal structure of PdSSe (especially the occupation of the S and Se atoms) and predict its properties based on the as-identified structure.

In the present work, we will address these issues by using the global structure search method combined with first-principles calculations. Three stable crystal structures with different occupations of the chalcogen atoms have been revealed for the bulk PdSSe. Furthermore, two stable polymorphs of monolayer PdSSe materials have been predicted by mechanical exfoliation of the bulk phase. In particular, monolayer PdSSe materials exhibit anisotropic mechanical performance, suitable band gaps, excellent light absorption capability, and ultrahigh carrier mobilities, which would endow them with further applications in photocatalysis, optoelectronics, and nanoelectronics.

II. Computational and analytical methods

Structure search simulations for the PdSSe system were performed by employing a particle swarm optimization algorithm as implemented in the CALYPSO code,[45–47] which is a global minimum search of the free energy surface. According to the previous experimental results and the unique structural characteristics of 2O phase PdX_2,[10,41] the chemical compositions were given as PdSSe, and the Pd atoms were fixed at the face centers and vertices of the orthogonal lattice, whereas the chalcogen atoms were allowed to move freely. In order to find out the lowest energy structure of the PdSSe bulk, we ran 30 generations for PdSSe and each generation produced 35 structures. The first generation was randomly generated, and 60% of the structures were produced from the previous generation by means of the local particle swarm optimization technique, and the remaining 40% of the structures were randomly generated to enhance the structural diversity. Geometry optimization, total energy, electronic structure, and optical property calculations were carried out mainly by using the Vienna Ab initio Simulation Package (VASP) code based on density functional theory (DFT).[48] The electron–ion interactions were described by projector-augmented-wave (PAW) potentials.[49,50] The generalized gradient approximation (GGA) was used to consider the exchange-dependent interaction with the Perdew–Burke–Ernzerhof (PBE) functional.[51] All computations employed a plane-wave cut-off energy of 520 eV. The Tkatchenko–Scheffler (TS) method was used to consider the interlayer vdW interactions (the choice of semiempirical correction methods is described in the ESI†).[52] Dipole corrections perpendicular to the monolayer have been taken into account because of the intrinsic dipole in the Janus structures.[42] During the geometry structure relaxations, k points of the reciprocal space were fixed to 0.02 $Å^{-1}$ in bulk, which were set to be $8 \times 8 \times 1$ in monolayer structures. A vacuum distance of 20 Å was used to avoid interactions between adjacent layers. To obtain accurate band gaps and optical absorption spectra, the Heyd–Scuseria–Ernzerhof (HSE06)[53,54] hybrid functional was also used to calculate the band structures and optical properties of the bulk and monolayer phases. The dynamic stability of the bulk (monolayer) phase was examined by calculating the phonon spectra for a $2 \times 2 \times 2$ ($4 \times 4 \times 1$) supercell with the PHONOPY code[55] interfaced with the density functional perturbation theory.[56] To evaluate the thermal stability of the monolayers, *ab initio* molecular dynamics (AIMD) simulations were performed by using the VASP code in the *NVT* ensemble. The $4 \times 4 \times 1$ supercell was constructed to reduce the constraints of periodic boundary conditions, and the simulations were carried out at a temperature of 300 K, for 5000 femtoseconds (fs) with a time step of 1 fs. A $3 \times 3 \times 1$ supercell

was adopted to simulate the interactions between the adsorbed molecules or atoms on the surface.

Based on the deformation potential theory,[57,58] the carrier mobility of the 2D PdSSe monolayer is calculated according to the following formula:

$$\mu_{2D} = \frac{e\hbar^3 C_{2D}}{K_B T m^* m_d (E_1^i)^2} \quad (1)$$

where $\hbar$ is the reduced Planck constant, K_B is the Boltzmann constant, m^* is the effective mass in the transport direction (both x and y), and m_d is the carrier average effective mass defined by $m_d = \sqrt{m_x^* m_y^*}$. T is the temperature, which is set to 300 K. E_1^i represents the deformation potential constant of the holes at the valence band maximum (VBM) or electrons at the conduction band minimum (CBM) along the transport direction, which is determined by $E_1^i = \Delta E/(\Delta l/l_0)$, where ΔE stands for the energy change of the CBM or VBM under compression or tensile strain, l_0 is the lattice constant along the deformation direction, and Δl is the deformation amount of l_0. C_{2D} is the in-plane elastic modulus of uniformly deformed 2D materials, which is defined by the formula $C_{2D} = [\partial^2 E/\partial \varepsilon^2]/S_0$, in which E is the total energy, ε is the applied strain, and S_0 is the area of the optimized unit cell.

In order to evaluate the absorptivity of the monolayer PdSSe, the imaginary part of the dielectric function is determined by summing the empty state of the equation:[59]

$$\varepsilon_{\alpha\beta}^2(\omega) = \frac{4\pi^2 e^2}{\Omega} \lim_{q\to 0} \frac{1}{q^2} \sum_{c,v,k} 2w_k \delta(\varepsilon_{ck} - \varepsilon_{vk} - \omega) \times u_{ck+e_\alpha q} | u_{vk} u_{ck+e_\beta q} | u_{vk}^* \quad (2)$$

The exponents c and v represent the conduction band and valence band states. u_{ck} is the cell periodic part of the orbitals at the k-point. The real part of the dielectric function is obtained from the imaginary part using the Kramers–Kronig relations. The optical absorption coefficient is defined as:

$$\alpha(\omega) = \sqrt{2}\frac{\omega}{c}\left[\sqrt{\varepsilon_1^2(\omega) + \varepsilon_2^2(\omega)} - \varepsilon_1(\omega)\right]^{\frac{1}{2}} \quad (3)$$

where ε_1 and ε_2 are the real and imaginary parts of the dielectric function, ω is the optical frequency, and c is the light speed in vacuum.

The Gibbs free energies (ΔG_H) are calculated to evaluate the hydrogen evolution reaction (HER) catalytic activity, which can be determined by

$$\Delta G_H = \Delta E_H + \Delta E_{ZPE} - T\Delta S \quad (4)$$

where ΔE_H is the adsorption energy, and ΔE_{ZPE} and ΔS are the differences of zero-point energy and entropy between the adsorbed state and the corresponding freestanding state. Given the fact that the vibrational entropy of the adsorbed state is very small, the entropy of adsorption of 1/2 H_2 is $\Delta S_H \cong -\frac{1}{2}S_H^0$, where S_H^0 is the entropy of H_2 in the gas phase under standard conditions. At 300 K, $T\Delta S_H$ is about 0.20 eV. ΔE_H and ΔE_{ZPE} are calculated by eqn (5) and (6), respectively.[60–63]

$$\Delta E_H = E_{(*+H)} - E_{(*)} - \frac{1}{2}E_{H_2} \quad (5)$$

$$\Delta E_{ZPE} = \Delta E_{ZPE}^H - \frac{1}{2}E_{ZPE}^{H_2} \quad (6)$$

In eqn (5), $E_{(*+H)}$, $E_{(*)}$, and E_{H_2} represent the total energy of a monolayer with one adsorbed H atom on the surface, the total energy of a monolayer, and the energy of a H_2 molecule in the gas phase, respectively. In eqn (6), ΔE_{ZPE}^H is the zero-point energy of the monolayer catalyst with one adsorbed H atom, while $E_{ZPE}^{H_2}$ is the zero-point energy of H_2 in the gas phase.

III. Results and discussion

III.1 Chemical structure, stability, and electronic structure of PdSSe in bulk phases

As shown in Fig. 1, the global structure search successfully screened three stable PdSSe from 1050 candidates, which are denoted as AA, AB, and BB, in the order of increasing energy (Table 1). These layered structures are constructed by A or B type monolayer PdSSe, and are stacked in different patterns.

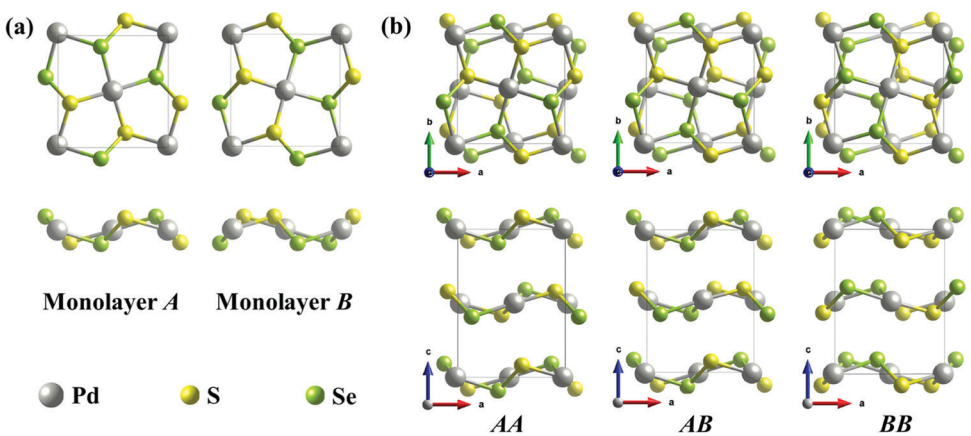

Fig. 1 Top and side views of the (a) monolayer and (b) bulk phase PdSSe. The bulk phases are formed by different stacking manners of the monolayer and are denoted as AA, AB, and BB.

The lattice constants obtained from geometry optimization are in good agreement with the experimental values.[41] The lattice constants and cell volumes increase from PdS_2 to PdSSe to $PdSe_2$, which are well consistent with the increasing atomic radius from S to Se. Notably, the chalcogen atoms (Se or S) of the same group are adjacent, and are located above and below the Pd atoms in monolayer A. By contrast, the Se and S atoms are located on different sides of the Pd atom, completely separated by the Pd layers in monolayer B. In fact, the monolayer B is a Janus structure, which has been artificially assumed in previous theoretical studies.[42] According to our theoretical predictions, although the BB bulk structure consisting of the Janus structure (monolayer B) is not the lowest energy one, its energy is comparable to those of the other two polymorphs (AA and AB). Therefore, we expect that these three bulk phases can exist simultaneously.

To assess the experimental feasibility of these predicted structures, we first calculate the formation energy to evaluate their thermodynamic stabilities. Previous experiments indicate that PdSSe can be prepared by sintering pressed powders of the mixed components (Pd, Se and S powders),[40,41] therefore the formation energy of PdSSe bulk is defined as $E_{form} = E_{PdSSe} - E_{Pd} - E_S - E_{Se}$, where E_{PdSSe} is the total energy of the PdSSe bulk per formula unit and E_{Pd}, E_S, and E_{Se} are the energies of the single Pd, S and Se atoms in their corresponding stable structures (Pd metal, S_8 and Se_8 molecular crystal were used). The formation energies are negative (Table 1), indicating that these three polymorphs of bulk phases indeed can be synthesized by an exothermic reaction from the constituents in their stable structures. In addition, as shown in Fig. S1 (ESI†), the dynamic stabilities of these three bulk phases are further confirmed using the phonon spectrum without any obvious imaginary frequency.

To obtain insight into the electronic properties of the bulk phases, we have calculated the band structure as well as their corresponding density of states. As shown in Fig. S2 (ESI†), the band dispersions are almost the same for these three bulk phases. Particularly, the electronic band structures show typical semimetallic characteristics at the PBE level, where the VBM is located at the Γ point, whereas the CBM is located on the S–Y path. Furthermore, the VBM and CBM are contributed mainly by the Pd 4d states and partially by S 3p and Se 4p states, which show a strong hybridization nature. The fundamental features of the band dispersions and the hybridization contribution of the electronic states for the PdSSe are essentially the same as the case of 2O phase PdS_2 and $PdSe_2$.[18,32,33,35] Obviously, the calculated semimetallic behavior is not consistent with the experimental measurement of semiconducting gaps for these 2O phase materials.[41] Therefore, the HSE06 screened Coulomb hybrid density functional is employed to calculate the band structure (Fig. 2), and indirect band gaps of 0.775, 0.700, and 0.617 eV are obtained for the AA, AB, and BB structures, respectively. The theoretically calculated band gap values of the 2O phase PdS_2 (0.818 eV),[33] PdSSe, and $PdSe_2$ (0.57 eV)[32] are close to the experimentally measured results, and coincide with the overall decreasing trend of the experimental data from PdS_2

Table 1 The optimized lattice constants, unit cell volume (V_0) and band gaps (E_g) of the three most stable polymorphs of PdSSe bulk phases compared with the experimental results. The relative energy E_r and the formation energy E_{form} of the predicted PdSSe, as well as available experimental data of the PdS_2 and $PdSe_2$ are given for comparison

	a (Å)	b (Å)	c (Å)	V_0 (Å^3)	E_g (eV)	E_r (meV per atom)	E_{form} (meV)
Exp.[41]	5.595	5.713	7.672	245.23	0.65[41]	—	—
AA	5.667	5.760	7.600	248.08	0.775	0	−820.28
AB	5.672	5.759	7.547	246.52	0.70	0.372	−819.17
BB	5.683	5.764	7.490	245.35	0.617	0.572	−818.57
PdS_2[10]	5.460	5.541	7.531	227.84	0.7–0.8[41]		
$PdSe_2$[10]	5.741	5.866	7.691	259.01	0.4[41]		

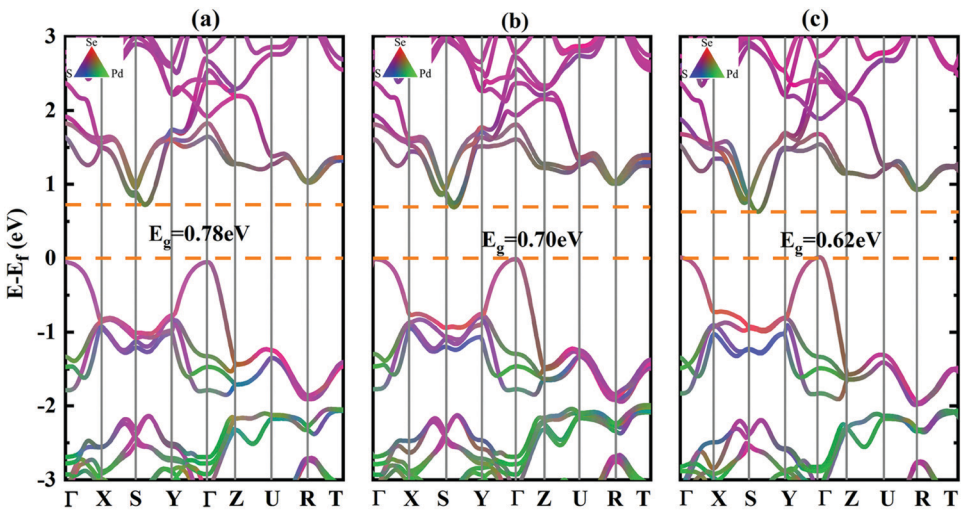

Fig. 2 The electronic band structures of (a) AA, (b) AB and (c) BB bulk phases calculated with HSE06. The color denotes the contributions from Se 4p (red), S 3p (blue) and Pd 4d (green) states, and strong hybridization between them. Dashed lines represent the Fermi level at 0 eV, and the band gaps E_g are shown between the VBM and CBM.

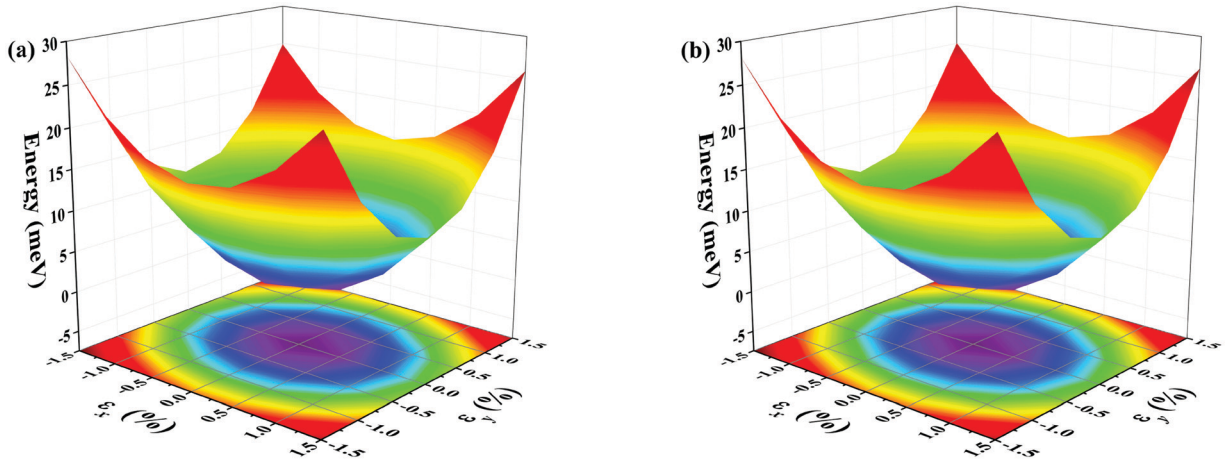

Fig. 3 The three-dimensional fitted surface plots of elastic energy *versus* strains along the *x* (ε_x) and *y* (ε_y) directions for (a) A and (b) B monolayer PdSSe.

to $PdSe_2$ (see Table 1).[41] Recognizing the similar electronic structure to the isostructural PdS_2 and $PdSe_2$, it is natural to speculate that these PdSSe materials will be potential high-performance candidates for electronic, optical, mechanical, and sensing applications.[7–9]

III.2 Exfoliation of 2D monolayer PdSSe from bulk phases

Theoretically, the interlayer interactions of the layered vdW materials are relatively small, and all layered NMDCs can be exfoliated from their bulk phases due to the low exfoliation energy ($E_{exfl.} < 1$ J m^{-2}).[7] Therefore, we examine the possibility of exfoliating the PdSSe monolayers from their corresponding bulk phases by calculating the exfoliation energy. The monolayer A can be cleaved from the AA or AB bulk phases, and monolayer B can be cleaved from the BB or AB bulk phases, respectively. The exfoliation energy of PdSSe monolayers is estimated from a six-layer bulk slab model.[64,65] When the interlayer distances are enlarged to about 6 Å, the exfoliation energies are converged (Fig. S3, ESI†). As shown in Table S3 (ESI†), the exfoliation energies of the monolayer PdSSe (0.33–0.34 J m^{-2}) are almost equal to those of isostructural monolayer PdS_2 and $PdSe_2$,[7] which satisfy the exfoliation energy criterion (below 1 J m^{-2}) for a feasible 2D material.[66] Therefore, the PdSSe monolayers have great probabilities to be exfoliated from their corresponding bulk phases.

The dynamic stability of these monolayers PdSSe is verified by calculating their phonon dispersion along the high-symmetry lines in the first Brillouin zone (Fig. S4, ESI†). There is no imaginary frequency in the phonon spectrum for these two monolayers, demonstrating that both A and B monolayers are dynamically stable. AIMD simulations are further performed to evaluate the thermal stabilities of these monolayers. In the whole simulation process, the average value of the total potential energy of the A supercell only increases by about 0.02 eV, and that of the B supercell is about 0.03 eV (Fig. S5, ESI†). In addition, as shown in Fig. S6 (ESI†), both the geometrical structures and chemical bonds only slightly deform but still maintain the pentagonal structure, confirming the thermal stability of the PdSSe monolayers.

We also examine the mechanical stability of the PdSSe monolayers by calculating the elastic energy $U(\varepsilon)$. By imposing small strains ε near the equilibrium positions, the elastic energy can be expressed as $U(\varepsilon) = E(\varepsilon) - E(0) = \frac{1}{2}U^{(2)}\varepsilon^2 + O(\varepsilon^3)$, where $E(\varepsilon)$ and $E(0)$ are the total energies of the system under strain ε and at a strain-free state, respectively.[67] $U^{(2)}$ is the expansion coefficient, determined by the elastic constants. The elastic energy $U(\varepsilon)$ of the 2D materials can be expressed as:[68]

$$U(\varepsilon) = \frac{1}{2}C_{11}{\varepsilon_{xx}}^2 + \frac{1}{2}C_{22}{\varepsilon_{yy}}^2 + C_{12}\varepsilon_{xx}\varepsilon_{yy} + 2C_{44}{\varepsilon_{xy}}^2 \quad (7)$$

In eqn (7), ε_{ij} are the infinitesimal strain tensors, and C_{ij} are the linear elastic constants. The values of elastic constants can be obtained from the energy surface of systems under different strains. Fig. 3 depicts the three-dimensional mesh of the elastic energy within the strain ranging from −1.5% to 1.5%. Both systems exhibit anisotropic responses in the *x* and *y* directions, which is in line with the puckered pentagonal structures of the monolayer PdSSe (Fig. 1). C_{ij} can be determined from a series of parabolic fittings of the $U(\varepsilon)$ with respect to uniaxial, biaxial and shear strains, which are shown in Fig. S7 (ESI†). All the calculated elastic constants are reported in Table 2. The elastic constants of the two monolayers are very similar, indicating that they have almost the same mechanical properties. The elastic constants satisfy the Born mechanical stability criteria:[69] $C_{44} > 0$ and $C_{11}C_{22} - {C_{12}}^2 > 0$, which indicates that these PdSSe monolayers are mechanically stable and would have strong resistance to the in-plane strains.

The mechanical properties are important for potential application of the monolayer materials. The in-plane Young's modulus (or in-plane stiffness) and Poisson's ratio are often used to describe the mechanical properties of 2D layered materials. The Young's

Table 2 Calculated elastic constants C_{ij} (N m^{-1}) of monolayers A and B

	C_{11}	C_{22}	$C_{11} + C_{22} + C_{12}$	C_{44}	C_{12}
A	46.14	69.57	120.13	5.37	4.42
B	46.08	69.62	120.19	5.39	4.49

modulus $E(\theta)$ and Poisson's ratio $\nu(\theta)$ along arbitrary directions can be deduced from the linear elasticity constant:[68]

$$E(\theta) = \frac{C_{11}C_{22} - C_{12}^2}{C_{11}s^4 + C_{22}c^4 + \left(\frac{C_{11}C_{22} - C_{12}^2}{C_{44}} - 2C_{12}\right)c^2s^2} \quad (8)$$

$$\nu(\theta) = \frac{\left(C_{11} + C_{22} - \frac{C_{11}C_{22} - C_{12}^2}{C_{44}}\right)c^2s^2 - C_{12}(c^4 + s^4)}{C_{11}s^4 + C_{22}c^4 + \left(\frac{C_{11}C_{22} - C_{12}^2}{C_{44}} - 2C_{12}\right)c^2s^2} \quad (9)$$

where θ is the angle relative to the x direction, $c = \cos\theta$ and $s = \sin\theta$. As shown in Fig. 4, the deviations of $E(\theta)$ and $\nu(\theta)$ from the perfect circles demonstrate the anisotropic mechanical properties, which result from the unique puckered pentagonal structure units of the monolayer PdSSe. The Young's modulus in the x and y directions is simplified to $E_x = (C_{11}C_{22} - C_{12}^2)/C_{22}$ and $E_y = (C_{11}C_{22} - C_{12}^2)/C_{11}$, and the corresponding Poisson's ratio is: $\nu_x = C_{12}/C_{22}$ and $\nu_y = C_{12}/C_{11}$. For monolayer A (B), the Young's modulus E_x = 45.86 (45.79) N m^{-1} and E_y = 69.15 (69.18) N m^{-1} and Poisson's ratio ν_x = 0.064 (0.064) and ν_y = 0.096 (0.097). The in-plane Young's modulus of the PdSSe monolayers is close to those of the monolayer PdS_2 and $PdSe_2$, but much lower than those of other typical 2D monolayers graphene (323 N m^{-1}) and MoS_2 (128 N m^{-1}), indicating that the PdSSe monolayers are rather flexible.[13,28] In line with previous results, the Young's modulus has a slightly reducing trend from PdS_2 to PdSSe, and to $PdSe_2$.[70] In addition, as shown in Fig. S8 (ESI†), the PdSSe monolayers can sustain a uniaxial strain up to 18% and 17% along the x and y directions, respectively, which are similar to those of the monolayer $PdSe_2$.[71] Moreover, significantly different ultimate strengths along the x and y directions imply that the PdSSe monolayers have anisotropic mechanical properties, which originated from the anisotropic pentagonal crystal structure. The in-plane Young's modulus and ideal strength indicate that the PdSSe monolayers exhibit highly flexible properties, which enable them to be used as flexible materials.

III.3 Electronic structure, optoelectronic, and catalytic properties of PdSSe monolayers

At the PBE level, both A and B PdSSe monolayers are indirect gap semiconductors with band gap values of 1.21 and 1.17 eV (Fig. S9, ESI†), in contrast to the semimetallic electronic structure of the bulk phases. The thickness-tunable band gap phenomenon has been observed in 2O phase $PdSe_2$, where the material changes from the bulk phase to monolayer accompanied by a semimetal to semiconductor transition.[9] In addition, GGA often tends to underestimate the band gap of semiconducting materials, and so we further calculate the electronic structure by using the HSE06 hybrid functional (Fig. 5). The band gap values increase to 2.10 and 2.06 eV for A and B monolayers, which are close to the theoretically calculated values of the monolayers PdS_2

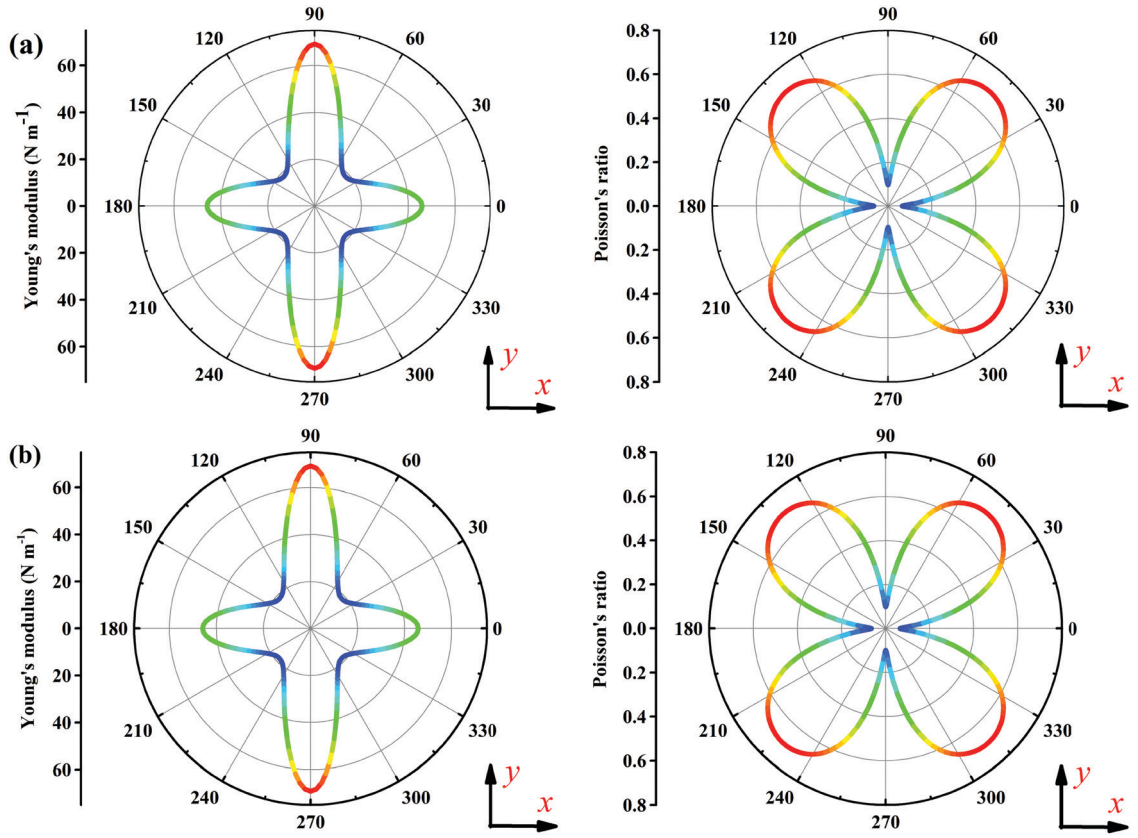

Fig. 4 Polar plots of the Young modulus $E(\theta)$ and Poisson's ratio $\nu(\theta)$ for monolayers A (a) and B (b). The red (high) and blue (low) colors denote the relative strength of the $E(\theta)$ and $\nu(\theta)$.

and $PdSe_2$.[70] As shown in Fig. 5, the projected band structure combined with the charge density plots indicates that the VBM mainly originates from the Se and S 4p states, while the CBM comes from the hybridization of the chalcogen p and Pd 4d states, which are similar to the case of monolayers PdS_2 and $PdSe_2$.[13,16] Considering the relatively heavy Pd element and broken symmetry of the 2D structure, we also investigate the effects of the spin–orbit coupling (SOC) on the band structure. The results obtained with and without SOC confirm that the SOC interactions have negligible influences (Fig. S9, ESI†), which will not change the properties studied in this paper, therefore SOC effects will be neglected in the following discussions.

The band gap values of both A and B monolayers are greater than 2 eV, which satisfy the minimum potential difference (1.23 eV) required for photocatalytic water splitting.[72,73] In addition to the value of the band gap, the band edge positions should also meet another important requirement of photocatalytic water splitting, that is the CBM (VBM) should be higher (lower) relative to the hydrogen reduction (water oxidation) potential of H^+/H_2 (H_2O/O_2). Therefore, their band edge positions are aligned with vacuum level corrections and compared with the reduction potential of hydrogen evolution and the oxidation potential of oxygen evolution. As shown in Fig. 6, the VBM is lower than the oxygen evolution potential (H_2O/O_2, −5.67 eV), while the CBM is higher than the hydrogen evolution potential (H^+/H_2, −4.44 eV), fulfilling the thermodynamic requirements for overall water splitting under acidic conditions (pH = 0).

It should be kept in mind that photocatalytic water splitting usually occurs in a neutral environment (pH = 7). Unfortunately, the positions of the CBM are lower than the reduction potential of hydrogen when pH = 7. A feasible method to manipulate the band edge positions is through band gap engineering by applying external strain. The band gap values of the PdSSe monolayers decrease with increasing tensile strain and increase with increasing compressive strain (Fig. S10, ESI†). Elastic strain has similar effects on the band gap of the two isostructural PdS_2 and $PdSe_2$ monolayer materials.[74] When subjected to a biaxial tensile (compressive) strain, the CBM pronouncedly shifts downward (upward), while the VBM changes slowly, resulting in the obvious decrease (increase) of band gap. Accordingly, the band gap of monolayer A (B) can be enlarged to 2.58 (2.57) eV under a biaxial compressive strain of −5%, and reduced to 1.51 (1.50) eV under a biaxial tensile strain of +5% (Fig. S10, ESI†). When the compressive strain is larger than 1%, the CBM positions shift up with the increasing compressive strain and exceed the hydrogen reduction potential, thereby fulfilling the requirements of an ideal photocatalyst for overall water splitting (Fig. 6).

As is known, the band gap values of the photocatalyst are very delicate. The band gap of the semiconductor is too large to

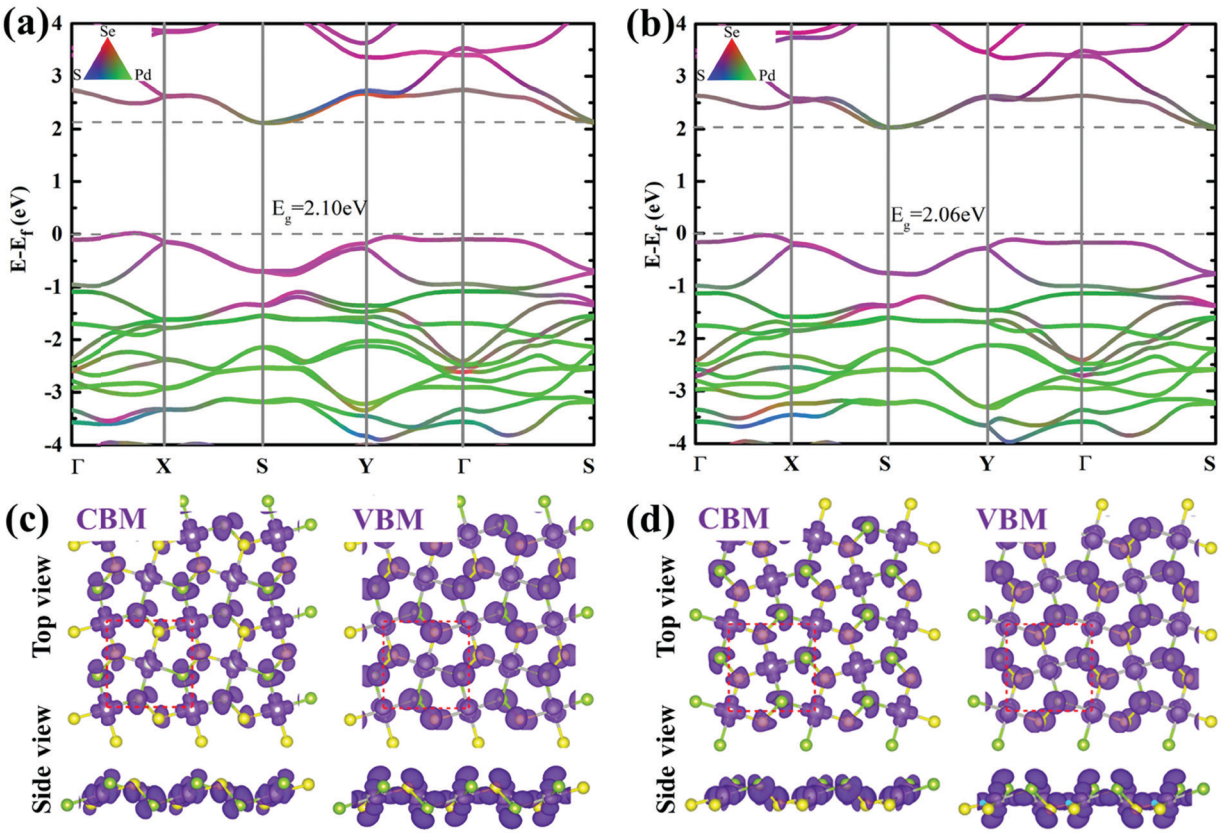

Fig. 5 The projected band structures of (a) A and (b) B monolayer PdSSe calculated with HSE06, which are projected onto Se 4p (red), S 3p (blue) and Pd 4d (green) states, respectively. The Fermi level is set to 0 eV. The corresponding real-space charge distribution of the VBM and CBM for A and B monolayer PdSSe is shown in (c) and (d); the iso-surface value is 0.005 e bohr^{-3}, with the dashed line representing the unit cell.

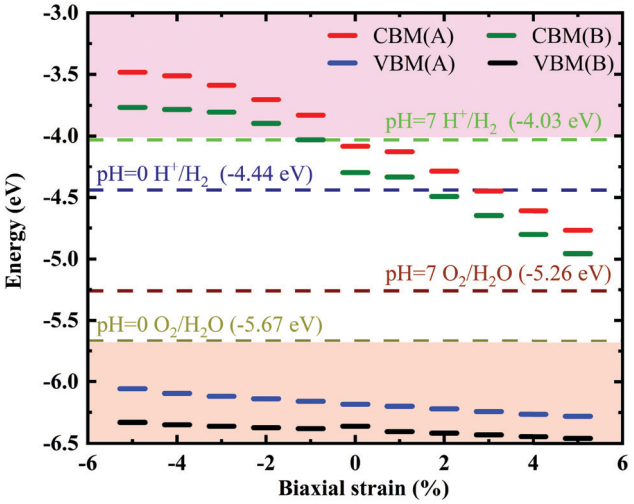

Fig. 6 Band edge positions of monolayers A and B as a function of biaxial strain. The positive (negative) values denote tensile (compressive) strains. The redox potentials are marked by the dashed lines for different pH values.

exploit the incident light adequately, while a narrow band gap leads to photo-generated carrier recombination.[75] Hence, it is hard to meet the above two conditions in a single material at the same time. Typical narrow band-gap semiconductors such as SiC, GaP, CdS, ZnO, TiO_2, WO_3 and $SrTiO_3$ have been widely studied as photocatalysts. However, the recombination probability of the photoexcited electron–hole pairs is quite high in the direct band-gap semiconductors, and the conduction band or valence band edge positions usually do not satisfy the water redox potentials in the water-splitting reactions (see Fig. S11, ESI†).[76] Alternatively, 2D materials have been proposed as potential candidates of photocatalysts for water splitting due to their tunable electronic properties. For example, black phosphorus (BP) and MoS_2 have been extensively studied for photocatalytic water splitting reactions because of their novel layered structure and excellent optoelectronic performance. However, the higher VBM position of BP and the lower CBM position of MoS_2 are obstacles for their practical application as photolytic water splitting materials in different pH environments (see Fig. S11, ESI†).[77] In addition, the direct band gaps of BP and MoS_2 are not conducive to reducing the carrier recombination rate. To construct heterojunctions or heterostructures can effectively adjust the band edge positions and light absorption performances.[78,79] Boron phosphide–blue phosphorene vdW heterostructures are extremely successful examples.[80] In addition, monolayer $PdSe_2$ has been demonstrated to be a potential candidate for photocatalytic water decomposition with appropriate band edge positions.[81] Present predictions indicate that elastic strain, as a clean and convenient method, effectively modulates the band gap and band edge positions of the PdSSe monolayers, which could facilitate its utilization in photocatalytic water splitting in different pH environments.

Besides the requirements of the band gap and band edge position, another important factor for an ideal photocatalyst is the light harvesting performance. As shown in Fig. 7, the PdSSe monolayers exhibit pronounced light absorption beginning at $\sim$2 eV, and the absorption coefficients reach the order of 10^6 cm^{-1}. Prominent absorption peaks can be observed in the visible-light and ultraviolet region, indicating the excellent light-harvesting capability. In the visible light range, the light absorption coefficients are much higher than those of MoS_2 and BP, which are comparable to those of $PdSe_2$ and PdS_2 (Fig. S12, ESI†). Furthermore, we present the optical properties of the PdSSe monolayers under biaxial strains in Fig. S13 (ESI†). Under the tensile strain, the peak value of the optical absorption coefficient decreases slightly, and the energy range corresponding to the absorption peak shows an obvious redshift. Under the compression strain, the absorption peak value decreases too, but the absorption range shows a blueshift. Considering the relationship between the potential energy surface and the band edge positions of the water splitting half reactions, it is suggested that compressed monolayers will always have a good ability to collect solar energy under both acidic and neutral conditions.

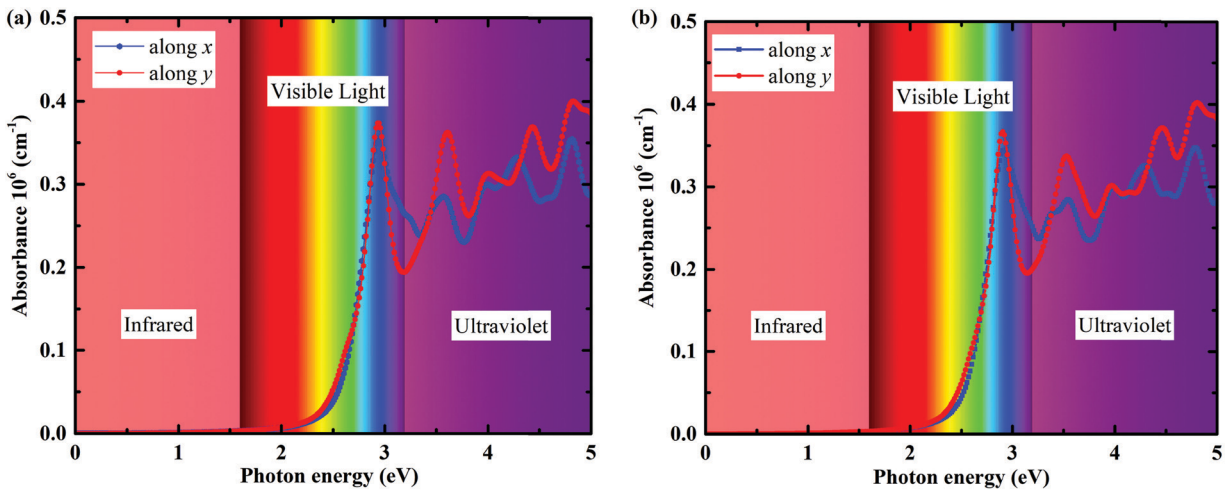

Fig. 7 The light absorption coefficient of (a) A and (b) B monolayer PdSSe.

Table 3 The effective mass (m^*), elastic modulus (C_{2D}), deformation potential constant (E_1^i), and carrier mobilities (μ) along the x and y directions for the monolayers PdSSe and PdX_2

Monolayer	Direction	Carrier	m^*/m_0	C_{2D} (J m^{-2})	E_1^i (eV)	μ (cm^2 V^{-1} s^{-1})
A	x	Electron	1.36	46.09	6.25	20.73
		Hole	1.54	46.09	0.76	831.73
	y	Electron	0.59	69.49	7.20	54.31
		Hole	1.17	69.49	1.20	653.02
B	x	Electron	2.16	46.04	7.01	5.85
		Hole	0.92	46.04	0.64	2520.44
	y	Electron	1.15	69.56	7.84	13.25
		Hole	1.17	69.56	1.15	928.50
PdS_2[13]	x	Electron	0.87	58	8.59	40.97
		Hole	0.72	58	2.12	339.25
	y	Electron	0.25	82	9.40	169.11
		Hole	1.75	82	3.11	91.73
$PdSe_2$[81]	x	Electron	1.88	38.44	5.24	29.40
		Hole	0.90	38.44	1.12	534.55
	y	Electron	0.49	98.18	5.03	229.01
		Hole	1.45	98.18	1.89	184.59

Furthermore, excellent carrier mobility is a consistent pursuit in the design of photocatalytic materials, to suppress the unfavorable electron–hole recombination.[78,80] Based on the deformation potential theory,[57,58] the carrier mobilities of the PdSSe monolayers are examined. Strains ranging from −1.5% (compressive) to 1.5% (tensile) are applied to the monolayers both in the x and y directions, respectively. The carrier effective masses (m^*) are obtained by second polynomial fitting to the VBM (hole) and CBM (electron). The in-plane elastic modulus C_{2D} in different transport directions is obtained through the quadratic function fitting the total energy of the system under strain (Fig. S14, ESI†). The deformation potential constants E_1^i along the transport directions are fitted by the shift of band edges induced by strain (Fig. S15, ESI†). Once the carrier effective masses, elastic modulus, and deformation potential constants are obtained, the carrier mobilities can be determined with eqn (1). The obtained effective masses (m^*), elastic modulus (C_{2D}), deformation potential constants (E_1^i), and carrier mobilities (μ) are summarized in Table 3.

According to the calculated results, the PdSSe monolayers exhibit considerable anisotropy in effective masses and elastic modulus. Particularly, the deformation potential constants of the electrons are much larger than that of the holes, which are consistent with the fact that the CBM is more susceptible to strain (Fig. 6). Due to the anisotropy of the effective masses, elastic modulus and deformation potential, the carrier mobilities of monolayer PdSSe show striking anisotropic characteristics. The hole mobility is much higher than the electron mobility in both x and y transport directions. In addition, there are great differences between the mobilities of electrons (20.73/54.31 cm^2 V^{-1} s^{-1}) and holes (831.73/653.02 cm^2 V^{-1} s^{-1}) along the same direction (x/y) in monolayer A. The anisotropy of the carrier mobilities is even more pronounced in monolayer B for electrons (5.85/13.25 cm^2 V^{-1} s^{-1}) and holes (2520.44/928.50 cm^2 V^{-1} s^{-1}) along the x/y direction. Remarkably, the significant anisotropy of the carrier mobilities mainly arises from the rather small deformation potential of the holes with respect to those of electrons, which matches well with previous results for other 2O phase PdX_2 monolayers.[13,15,28,81]

The anisotropic ratio is a key parameter to evaluate the mobility anisotropy, which is defined as: $R_{ani} = \mu_{max}/\mu_{min}$, where μ_{max} and μ_{min} are the maximum and minimum carrier mobility for electrons and holes, respectively.[16,82] Along the same transport direction, the calculated R_{ani} of the hole/electron mobility ratio is as high as 40.12/430.99 (12.02/70.08) along the x (y) direction for the A/B monolayer, indicating that the carriers of electrons and holes are significantly separated in both transport directions. Compared to the potential photocatalysts PdX_2,[13,81] the monolayer of PdSSe shows much more pronounced anisotropy of mobility (Table 3). The carriers' mobility anisotropy can promote the separation of the photogenerated electrons and holes, and effectively reduce the probability of recombination, which can remarkably promote the photocatalytic water splitting. Furthermore, such ultrahigh carrier mobilities and hole/electron mobility ratio are beneficial for high-performance nanoelectronic devices.

The adsorption of water molecules is a prerequisite in the process of photocatalytic water splitting. We calculated the adsorption energies of the water molecules at different absorption sites: approximate top position of the Pd and X atoms, the middle of Pd–X and X–X bonds, and the hollow of the pentagons (Fig. S16, ESI†). The adsorption energy is defined as: $E_a = E_{(PdSSe+H_2Omolecule)} - E_{PdSSe} - E_{H_2O}$, where $E_{(PdSSe+H_2Omolecule)}$, E_{PdSSe}, and E_{H_2O} are the energies of the adsorbate-PdSSe equilibrium system, isolated PdSSe monolayer, and isolated H_2O molecule, respectively. The calculated results indicate that the largest negative adsorption energies for H_2O molecules are −0.133 and −0.162 eV for the A and B monolayers (Table S4, ESI†). The water molecules prefer the stably adsorbed sites on top of the Se atom for A and the Pd–Se bond for B, as shown in Fig. S17 (ESI†). For the HER, the reaction energy barriers (ΔG_H) are 1.64 eV for A and 1.55 eV for the B monolayer (Fig. 8). The ΔG_H of both A and B monolayers is higher than that of $PdSe_2$ (1.175 eV),[81] but lower than that of the Janus WSSe (~1.82 eV) and 2H-MoS_2 (2 eV).[83] Such high Gibbs free energies imply that the PdSSe monolayer surfaces are inert in the HER, which is not conducive to proton and

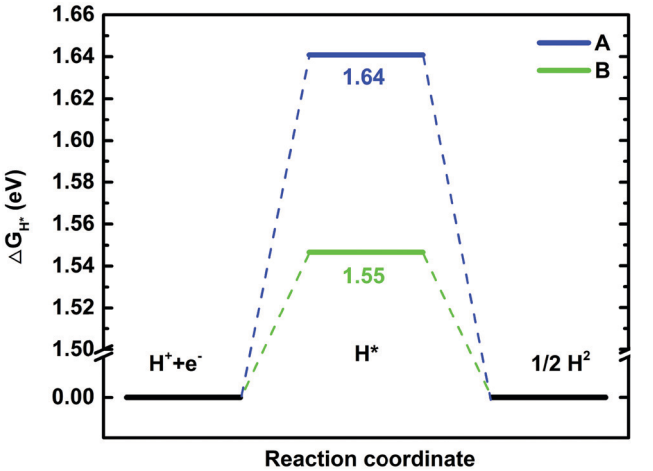

Fig. 8 The Gibbs free energies of the HER under standard conditions for monolayers A and B.

electron transfer.[84] It has been shown that the Janus WSSe monolayer can achieve a ΔG_H of -15 meV by introducing Se-vacancies.[83] By fine-tuning the strain and vacancy ratio or doping Pt atoms, a ΔG_H of ~ 0 eV can even be achieved in monolayer 2H-MoS_2.[79,85] Therefore, we expect to modulate the HER activity of the monolayer PdSSe by introducing vacancies, doping, and strain engineering. Excellent mechanical properties, light absorption performance, and ultrahigh carrier-mobility anisotropy enable PdSSe monolayers to be promising candidates for flexible electronics, optoelectronics, photocatalytic water splitting, and nanoelectronics.

IV. Conclusion

To summarize, we successfully identified the ground-state structure of PdSSe using a global structure search combined with first-principles DFT calculations. Moreover, two types of monolayer PdSSe can be exfoliated from the bulk phases, which are found to be dynamically, thermally, and mechanically stable using phonon spectra and AIMD simulations, as well as elastic moduli calculations. In addition, our HSE06 calculation shows that both kinds of monolayers are semiconductors with tunable band gap values in the visible-light region. Furthermore, the band edge positions of the monolayer PdSSe fulfill the requirements of photocatalytic water splitting. In addition, the monolayer PdSSe shows excellent light harvesting performance and anisotropic ultrahigh carrier mobility. These outstanding properties enable PdSSe to be a promising candidate material for applications in photocatalysis, photoconversion and nanoelectronic devices. Our theoretical results would stimulate the experimental synthesis of 2D PdSSe and extend the pentagonal 2D NMDC systems, which could greatly enrich the diversity and advance the applications of NMDC materials.

Conflicts of interest

There are no conflicts to declare.

Acknowledgements

The work was sponsored by the National Natural Science Foundation of China (No. 11864008) and the Guangxi Natural Science Foundation (No. 2018GXNSFAA138185, 2018AD19200 and 2019GXNSFGA245006).

References

1 K. S. Novoselov, *et al.*, Electric field effect in atomically thin carbon films, *Science*, 2004, **306**, 666–669.
2 A. H. C. Neto, *et al.*, The electronic properties of graphene, *Rev. Mod. Phys.*, 2009, **81**, 109.
3 S. Das, *et al.*, Beyond graphene: progress in novel two-dimensional materials and van der Waals solids, *Annu. Rev. Mater. Res.*, 2015, **45**, 1–27.
4 Q. H. Wang, *et al.*, Electronics and optoelectronics of two-dimensional transition metal dichalcogenides, *Nat. Nanotechnol.*, 2012, **7**, 699–712.
5 Y. Xiao, M. Zhou, J. Liu, J. Xu and L. Fu, Phase engineering of two-dimensional transition metal dichalcogenides, *Sci. China Mater.*, 2019, **62**, 759–775.
6 S. Manzeli, *et al.*, 2D transition metal dichalcogenides, *Nat. Rev. Mater.*, 2017, **2**, 17033.
7 R. Kempt, A. Kuc and T. Heine, Two-Dimensional Noble-Metal Chalcogenides and Phosphochalcogenides, *Angew. Chem., Int. Ed.*, 2020, **59**, 2–15.
8 L. Pi, *et al.*, Recent Progress on 2D Noble-Transition-Metal Dichalcogenides, *Adv. Funct. Mater.*, 2019, **29**, 1904932.
9 E. Chen, *et al.*, 2D layered noble metal dichalcogenides (Pt, Pd, Se, S) for electronics and energy applications, *Mater. Today Adv.*, 2020, **7**, 100076.
10 F. Grønvold and E. Røst, The crystal structure of $PdSe_2$ and PdS_2, *Acta Crystallogr.*, 1957, **10**, 329–331.
11 P. Miró, M. Ghorbani-Asl and T. Heine, Two dimensional materials beyond MoS_2: noble-transition-metal dichalcogenides, *Angew. Chem., Int. Ed.*, 2014, **53**, 3015–3018.
12 J. Sun, *et al.*, Electronic, transport, and optical properties of bulk and mono-layer $PdSe_2$, *Appl. Phys. Lett.*, 2015, **107**, 153902.
13 Y. Wang, Y. Li and Z. Chen, Not your familiar two dimensional transition metal disulfide: structural and electronic properties of the PdS_2 monolayer, *J. Mater. Chem. C*, 2015, **3**, 9603–9608.
14 M. Ghorbani-Asl, *et al.*, A single-material logical junction based on 2D crystal PdS_2, *Adv. Mater.*, 2016, **28**, 853–856.
15 D. Qin, *et al.*, Monolayer $PdSe_2$: A promising two-dimensional thermoelectric material, *Sci. Rep.*, 2018, **8**, 2764.
16 W. Lei, *et al.*, A new 2D high-pressure phase of $PdSe_2$ with high-mobility transport anisotropy for photovoltaic applications, *J. Mater. Chem. C*, 2019, **7**, 2096–2105.
17 A. D. Oyedele, *et al.*, $PdSe_2$: pentagonal two-dimensional layers with high air stability for electronics, *J. Am. Chem. Soc.*, 2017, **139**, 14090–14097.
18 Y. Zhao, *et al.*, Low-Symmetry $PdSe_2$ for High Performance Thermoelectric Applications, *Adv. Funct. Mater.*, 2020, 2004896.
19 P. K. Cheng, *et al.*, Passively Q-switched and femtosecond mode-locked erbium-doped fiber laser based on a 2D palladium disulfide (PdS_2) saturable absorber, *Photonics Res.*, 2020, **8**, 511–518.
20 L.-S. Lu, *et al.*, Layer-Dependent and In-Plane Anisotropic Properties of Low-Temperature Synthesized Few-Layer $PdSe_2$ Single Crystals, *ACS Nano*, 2020, **14**, 4963–4972.
21 A. N. Hoffman, *et al.*, Exploring the air stability of $PdSe_2$ via electrical transport measurements and defect calculations, *npj 2D Mater. Appl.*, 2019, **3**, 1–7.
22 Q. Liang, *et al.*, High-Performance, Room Temperature, Ultra-Broadband Photodetectors Based on Air-Stable $PdSe_2$, *Adv. Mater.*, 2019, **31**, 1807609.
23 Y. Gu, *et al.*, Two-Dimensional Palladium Diselenide with Strong In-Plane Optical Anisotropy and High Mobility Grown by Chemical Vapor Deposition, *Adv. Mater.*, 2020, 1906238.

24 L.-H. Zeng, *et al.*, Controlled synthesis of 2D palladium diselenide for sensitive photodetector applications, *Adv. Funct. Mater.*, 2019, **29**, 1806878.
25 W. L. Chow, *et al.*, High mobility 2D palladium diselenide field-effect transistors with tunable ambipolar characteristics, *Adv. Mater.*, 2017, **29**, 1602969.
26 A. Di Bartolomeo, *et al.*, Pressure-tunable ambipolar conduction and hysteresis in thin palladium diselenide field effect transistors, *Adv. Funct. Mater.*, 2019, **29**, 1902483.
27 S. Ahmad and G. Schreckenbach, *Ab initio* study of strain and electric field dependent variation in electronic and thermoelectric properties of PdS_2, *Mater. Today Commun.*, 2020, **24**, 100976.
28 Y.-S. Lan, *et al.*, Penta-PdX_2 (X = S, Se, Te) monolayers: promising anisotropic thermoelectric materials, *J. Mater. Chem. A*, 2019, **7**, 11134–11142.
29 A. Di Bartolomeo, *et al.*, Electron irradiation of multilayer $PdSe_2$ field effect transistors, *Nanotechnology*, 2020, **31**, 375204.
30 J. Lin, *et al.*, Novel Pd_2Se_3 Two-dimensional phase driven by interlayer fusion in layered $PdSe_2$, *Phys. Rev. Lett.*, 2017, **119**, 016101.
31 A. D. Oyedele, *et al.*, Defect-mediated phase transformation in anisotropic two-dimensional $PdSe_2$ crystals for seamless electrical contacts, *J. Am. Chem. Soc.*, 2019, **141**, 8928–8936.
32 W. Lei, *et al.*, Ferroelastic lattice rotation and band-gap engineering in quasi 2D layered-structure $PdSe_2$ under uniaxial stress, *Nanoscale*, 2019, **11**, 12317–12325.
33 W. Lei, *et al.*, Structural transition, metallization, and superconductivity in quasi-two-dimensional layered PdS_2 under compression, *Phys. Rev. B*, 2020, **101**, 205149.
34 M. A. ElGhazali, *et al.*, Pressure-induced metallization, transition to the pyrite-type structure, and superconductivity in palladium disulfide PdS_2, *Phys. Rev. B*, 2019, **100**, 014507.
35 M. A. ElGhazali, *et al.*, Pressure-induced superconductivity up to 13.1 K in the pyrite phase of palladium diselenide $PdSe_2$, *Phys. Rev. B*, 2017, **96**, 060509.
36 P. Lv, G. Tang and Y. Liu, *et al.*, van der Waals direction transformation induced by shear strain in layered $PdSe_2$, *Extreme Mech. Lett.*, 2021, **44**, 101231.
37 M. Fu, *et al.*, Defects in Highly Anisotropic Transition-Metal Dichalcogenide $PdSe_2$, *J. Phys. Chem. Lett.*, 2019, **11**, 740–746.
38 Q. Liang, *et al.*, Performance Improvement by Ozone Treatment of 2D $PdSe_2$, *ACS Nano*, 2020, **14**, 5668–5677.
39 Q. Liang, *et al.*, Oxygen-induced controllable p-type doping in 2D semiconductor transition metal dichalcogenides, *Nano Res.*, 2020, **13**, 3439–3444.
40 J. H. Ryu, *et al.*, Compositional effect in pentagonal layered $PdSe_{2-x}S_x$ solid-solutions and their transport properties, *Scr. Mater.*, 2020, **182**, 6–10.
41 F. Hulliger, Electrical properties of some nickel-group chalcogenides, *J. Phys. Chem. Solids*, 1965, **26**, 639–645.
42 Y. Zhou, X. Yang and J. He, PdSSe: Two-dimensional pentagonal Janus structures with strong visible light absorption for photovoltaic and photocatalytic applications, *Vacuum*, 2020, **181**, 109649.
43 E. A. Moujaes and W. A. Diery, Thermoelectric properties of 1 *T* monolayer pristine and Janus Pd dichalcogenides, *J. Phys.: Condens. Matter*, 2019, **31**, 455502.
44 W.-L. Tao, *et al.*, Thermoelectric properties of Janus MXY (M = Pd, Pt; X, Y = S, Se, Te) transition-metal dichalcogenide monolayers from first principles, *J. Appl. Phys.*, 2020, **127**, 035101.
45 Y. Wang, *et al.*, Crystal structure prediction via particle-swarm optimization, *Phys. Rev. B: Condens. Matter Mater. Phys.*, 2010, **82**, 094116.
46 Y. Wang, *et al.*, CALYPSO: A method for crystal structure prediction, *Comput. Phys. Commun.*, 2012, **183**, 2063–2070.
47 Bo Gao, *et al.*, Interface structure prediction via CALYPSO method, *Sci. Bull.*, 2019, **64**, 301–309.
48 G. Kresse and J. Furthmüller, Efficient iterative schemes for *ab initio* total-energy calculations using a plane-wave basis set, *Phys. Rev. B: Condens. Matter Mater. Phys.*, 1996, **54**, 11169.
49 P. E. Blöchl, Projector augmented-wave method, *Phys. Rev. B: Condens. Matter Mater. Phys.*, 1994, **50**, 17953.
50 G. Kresse and D. Joubert, From ultrasoft pseudopotentials to the projector augmented-wave method, *Phys. Rev. B: Condens. Matter Mater. Phys.*, 1999, **59**, 1758.
51 J. P. Perdew, K. Burke and M. Ernzerhof, Generalized gradient approximation made simple, *Phys. Rev. Lett.*, 1996, **77**, 3865.
52 A. Tkatchenko and M. Scheffler, Accurate molecular van der Waals interactions from ground-state electron density and free-atom reference data, *Phys. Rev. Lett.*, 2009, **102**, 073005.
53 J. Heyd, E. S. Gustavo and M. Ernzerhof, Hybrid functionals based on a screened Coulomb potential, *J. Chem. Phys.*, 2003, **118**, 8207–8215.
54 A. V. Krukau, *et al.*, Influence of the exchange screening parameter on the performance of screened hybrid functionals, *J. Chem. Phys.*, 2006, **125**, 224106.
55 A. Togo and I. Tanaka, First principles phonon calculations in materials science, *Scr. Mater.*, 2015, **108**, 1–5.
56 S. Baroni, *et al.*, Phonons and related crystal properties from density-functional perturbation theory, *Rev. Mod. Phys.*, 2001, **73**, 515.
57 J. Bardeen and W. Shockley, Deformation potentials and mobilities in non-polar crystals, *Phys. Rev.*, 1950, **80**, 72.
58 S. Bruzzone and G. Fiori, *Ab initio* simulations of deformation potentials and electron mobility in chemically modified graphene and two-dimensional hexagonal boron-nitride, *Appl. Phys. Lett.*, 2011, **99**, 222108.
59 M. Gajdoš, *et al.*, Linear optical properties in the projector-augmented wave methodology, *Phys. Rev. B: Condens. Matter Mater. Phys.*, 2006, **73**, 045112.
60 J. K. Nørskov, T. Bligaard and A. Logadottir, *et al.*, Trends in the exchange current for hydrogen evolution, *J. Electrochem. Soc.*, 2005, **152**, J23.
61 Z. H. Liu, C. L. Yang and M. S. Wang, *et al.*, SiI_2 monolayer as a promising photocatalyst for water splitting hydrogen production under the irradiation of solar light, *Int. J. Hydrogen Energy*, 2020, **45**, 17517–17524.
62 H. Y. Liu, C. L. Yang and M. S. Wang, *et al.*, Two-dimensional hexaphosphate $BiMP_6$ (M = Al, Ga, In) with desirable band gaps and ultrahigh carrier mobility for

photocatalytic hydrogen evolution, *Appl. Surf. Sci.*, 2020, **517**, 146166.

63 H. Y. Liu, C. L. Yang and M. S. Wang, *et al.*, 2D AlP_3 with high carrier mobility and tunable band structure, *J. Phys.: Condens. Matter*, 2019, **32**, 055001.

64 T. Gould, S. Lebègue and J. F. Dobson, Dispersion corrections in graphenic systems: a simple and effective model of binding, *J. Phys.: Condens. Matter*, 2013, **25**, 445010.

65 E. Ziambaras, *et al.*, Potassium intercalation in graphite: a van der Waals density-functional study, *Phys. Rev. B: Condens. Matter Mater. Phys.*, 2007, **76**, 155425.

66 K. Choudhary, *et al.*, High-throughput Identification and Characterization of Two-dimensional Materials using Density functional theory, *Sci. Rep.*, 2017, **7**, 1–16.

67 Y. Ding and Y. Wang, Density functional theory study of the silicene-like SiX and XSi_3 (X = B, C, N, Al, P) honeycomb lattices: the various buckled structures and versatile electronic properties, *J. Phys. Chem. C*, 2013, **117**, 18266–18278.

68 E. Cadelano, *et al.*, Elastic properties of hydrogenated graphene, *Phys. Rev. B: Condens. Matter Mater. Phys.*, 2010, **82**, 235414.

69 M. Born and K. Huang, *Dynamical theory of crystal lattices*, Clarendon Press, 1954.

70 W. Xiong, K. Huang and S. Yuan, The mechanical, electronic and optical properties of two-dimensional transition metal chalcogenides MX_2 and M_2X_3 (M = Ni, Pd; X = S, Se, Te) with hexagonal and orthorhombic structures, *J. Mater. Chem. C*, 2019, **7**, 13518–13525.

71 G. Liu, Q. Zeng, P. Zhu, R. Quhe and P. Lu, Negative Poisson's ratio in monolayer $PdSe_2$, *Comput. Mater. Sci.*, 2019, **160**, 309–314.

72 S. Chen and L.-W. Wang, Thermodynamic oxidation and reduction potentials of photocatalytic semiconductors in aqueous solution, *Chem. Mater.*, 2012, **24**, 3659–3666.

73 H. L. Zhuang and R. G. Hennig, Single-layer group-III monochalcogenide photocatalysts for water splitting, *Chem. Mater.*, 2013, **25**, 3232–3238.

74 S. Deng, L. Li and Y. Zhang, Strain modulated electronic, mechanical, and optical properties of the monolayer PdS_2, $PdSe_2$, and $PtSe_2$ for tunable devices, *ACS Appl. Nano Mater.*, 2018, **1**, 1932–1939.

75 K. Zheng, *et al.*, Two-dimensional penta-$SiAs_2$: a potential metal-free photocatalyst for overall water splitting, *J. Mater. Chem. C*, 2020, **8**, 11980–11987.

76 H. Tong, S. Ouyang, Y. Bi, N. Umezawa, M. Oshikiri and J. Ye, Nano-photocatalytic materials: possibilities and challenges, *Adv. Mater.*, 2012, **24**, 229–251.

77 W. Hu, L. Lin, R. Zhang, C. Yang and J. Yang, Highly Efficient Photocatalytic Water Splitting over Edge-Modified Phosphorene Nanoribbons, *J. Am. Chem. Soc.*, 2017, **139**, 15429–15436.

78 X. Zhang, Z. Zhang and D. Wu, *et al.*, Computational screening of 2D materials and rational design of heterojunctions for water splitting photocatalysts, *Small Methods*, 2018, **2**, 1700359.

79 X. Zhang, A. Chen and L. Chen, *et al.*, 2D Materials Bridging Experiments and Computations for Electro/Photocatalysis, *Adv. Energy Mater.*, 2021, 2003841.

80 I. Shahid, S. Ahmad and N. Shehzad, *et al.*, Electronic and photocatalytic performance of boron phosphide-blue phosphorene vdW heterostructures, *Appl. Surf. Sci.*, 2020, **523**, 146483.

81 C. Long, Y. Liang, H. Jin, B. Huang and Y. Dai, $PdSe_2$: flexible two-dimensional transition metal dichalcogenides monolayer for water splitting photocatalyst with extremely low recombination rate, *ACS Appl. Energy Mater.*, 2018, **2**, 513–520.

82 Y. Jing, *et al.*, Ultrathin layers of PdPX (X = S, Se): two dimensional semiconductors for photocatalytic water splitting, *Chem. – Eur. J.*, 2017, **23**, 13612–13616.

83 D. Er, H. Ye and N. C. Frey, *et al.*, Prediction of enhanced catalytic activity for hydrogen evolution reaction in Janus transition metal dichalcogenides, *Nano Lett.*, 2018, **18**, 3943–3949.

84 C. Ling, L. Shi and Y. Ouyang, *et al.*, Nanosheet supported single-metal atom bifunctional catalyst for overall water splitting, *Nano Lett.*, 2017, **17**, 5133–5139.

85 H. Li, C. Tsai and A. L. Koh, *et al.*, Activating and optimizing MoS_2 basal planes for hydrogen evolution through the formation of strained sulphur vacancies, *Nat. Mater.*, 2016, **15**, 48–53.

